This Article is under Formatting, the PDF's ready file will be replaced soon.

Thermo-Mechanical Behavior and Intelligent Optimization of Contact Temperature During Ultrasonic Vibration-Assisted Single-Pole Magnetic Abrasive Finishing of Zinc Alloy

Authors

Devesh Ojha[1], Rajendra Kumar Srivastava[2]*

*[1]*Assistant Professor, Department of Civil Engineering, Amity University, Lucknow, India*

[2]Professor, Department of Civil Engineering, Motilal Nehru National Institute of Technology, Allahabad, India

Corresponding Author's Email: *dojha@lko.amity.edu*

ABSTRACT

This study proposes a new integration of the experimental analysis, multi-physics finite element modelling (FEM) and machine learning (ML) optimisation of contact temperature (CT) in ultrasonic vibration-assisted single pole magnetic abrasive finishing (UV-SPMAF) of zinc alloy. The three gaps of the research are addressed: (i) The absence of a multi-physics FEM model that can couple electromagnetic, thermal and structural fields for UV-SPMAF of zinc; (ii) No quantified contribution of the ultrasonic frequency and amplitude to CT; and (iii) No ML-driven predictive model for CT in this hybrid process. The L-18 Taguchi orthogonal array was used, which contained six parameters: tool speed (250–1250 RPM), working gap (4–6 mm), feed rate (1.5–5.5 mm/s), pulse on time (1–5 min), ultrasonic frequency (20–40 kHz), and amplitude (5–15 µm). ANOVA revealed that working gap (44.21%) and tool speed (34.33%) were dominant factors, while UV frequency (4.16%) and amplitude (2.84%) are statistically significant ($p < 0.05$). UV assistance gives a decrease in CT of 6.5–9.1% and an increase in the surface roughness of up to 14.2%. The periodic shear-stress relief occurs under UV vibrations as confirmed by FEM ($R^2 = 0.961$, RMSE = 0.31°C). For the prediction of CT, $R^2 = 0.9814$ was obtained by ANN. Optimal parameters yield CT = 25.71 ± 0.48°C with 51.72% SR improvement. The resultant surface is found to have uniform micro-strains by SEM and XRD.

Keywords: *UV-SPMAF; contact temperature; FEM; ANN; zinc alloy; ANOVA; Taguchi; surface roughness; thermal management.*

1. INTRODUCTION

The functional performance, corrosion resistance and dimensional accuracy of precision engineering components is determined by the surface quality. Regular finishing techniques cannot produce sub-micrometer surface roughness without thermal damage and/or residual tensile stresses [1,2]. Magnetic abrasive finishing (MAF) is a process that uses flexible magnetic abrasive brushes (FMAB), which are pressed against the surface of workpieces, to cause progressive micro-cutting to sub-micrometre levels [1,3,4]. Single pole MAF (SPMAF) is simpler to integrate with CNC [5,6]. The application of hybridisation with ultrasonic vibration (UV-SPMAF) results in improvement of the particle penetration depth, contact arc width and cutting-edge renewal, at the same time improving the material removal rate and surface finish [7,8,9,10].

The generation of heat during the finishing operation at the workpiece-tool interface is an important consideration often overlooked. Thermal softening, oxide formation, stress reversal and micro-crack nucleation [11,12,13,14] are all processes that occur at elevated contact temperatures. Zinc has a high thermal conductivity (116 W/m·K) and is thermally sensitive and is being used in many applications including die-casting, galvanising, MEMS and biomedical packaging [15,16]. However, to the best of our knowledge, there has been no study that combines FEM (multi-physics simulation) and modelling with ML for optimizing thermal behavior of UV-SPMAF of zinc. Three specific research gaps are solved: (i) No coupled FEM model for UV-SPMAF of zinc; (ii) No quantitative ultrasonic parameter CT contribution data; And (iii) No ANN based CT predictor for UV-SPMAF. These are solved by using L-18 Taguchi experiment, multi physics FEM, ANN modelling and SEM/XRD characterisation.

2. LITERATURE REVIEW

2.1 MAF Fundamentals

Shinmura et al. [1] have introduced magnetic-force-generated finishing pressure controls micro-cutting, which decreases the Ra from micrometre to nanometre level. Yamaguchi and Shinmura [2] correlated uniform flux density with uniform SR and Jain et al. [3] reported the evolution of three phases at surface. Chang et al. [4] suggested two-step abrasive approach. Ra = 10 nm has been achieved by the surface of metallic mirror material, as proved by Mori et al. [17]. The highest SR improvement from Judal and Yadava [18] in hybrid electrochemical-MAF of 95%.

2.2 Ultrasonic-Assisted MAF

Mulik and Pandey [8,19] demonstrated that MRR and surface quality are much higher with unbonded SiC using UA-MAF, which was due to periodic FMAB separation, thereby lowering the specific cutting force. Rana et al. [9] demonstrated that the sintered powders are more effective than mixed powders in UA-MAF. Optimization of six UA-MAF parameters was done using RSM to gain sevenfold (78%) improvement in SR by Dhull et al. [18,19]. Singh and Walia [20] proposed a theory for the statistics of vibration trajectory in which they assumed that the ratio of vibration velocity to cutting velocity determines the statistics of the abrasive trajectory.

2.3 Contact Temperature in MAF

Mishra et al. [21] laid the groundwork for MAF CT model. Singh et al. [22] have demonstrated that the spindle speed caused a temperature rise and working gap caused a temperature drop by FEM. Sharma et al. [5] made the first SPMAF CT measurements on silicon wafers. Li et al. [23] found that UV vibrations in stainless steel MAF will decrease the peak CT through the redistribution of heat. Zhang et al. [15] created a multi-physics model for the zinc MAF, which also did not consider the effect of UV.

2.4 Machine Learning in MAF

Choopani et al. [24] showed that ANN has better ability to predict nonlinear MRR than RSM. Kaur et al. [25] achieved $R^2 > 0.97$ for SR prediction. Malhotra et al. [26] used deep learning for the prediction of CT and achieved 94% thermal excursion detection. There is no ANN CT model for UV-SPMAF of zinc. [Table 1]

2.5 Research Gap Summary — Table 1

Table 1. Summary of relevant literature and identified research gaps in UV-SPMAF thermal analysis.

Ref.	Material	Process	Key Parameter	Gap Identified	Remark
[1]	Steel	MAF	Finishing pressure	No thermal analysis	Pioneer micro-cutting mechanics
[7]	Ti alloy	V-MAF	Vibration mode	No CT data reported	3-mode vibration comparison
[23]	Steel	MAF	Interface temp.	No ultrasonic assist	Analytical thermal model
[24]	Al 6060	MAF–FEM	Temp. distribution	No UV+MAF hybrid	FEM simulation only
[5]	Si wafer	SPMAF	Work-brush temp.	Zinc not studied	First SPMAF CT study
[8]	Steel	UA-MAF	Unbonded SiC	No CT prediction	Unbonded abrasive hybrid
[29]	Ti alloy	UV-MAF	Tool feed UV	No thermal coupling	Axial UV assistance
[12]	Al alloy	UV-SPMAF	Thermal effects	No multi-physics FEM	Partial thermal study
[15]	Zinc	MAF	Temp./stress	No UV in model	Multi-physics; no UV
[30]	Zinc	UV-SPMAF	CT measurement	No FEM+ANN model	Baseline: present work extends

A quantitative, criterion-by-criterion comparison of the present study against these and additional UV-assisted/hybrid MAF studies is provided later in Section 5.7 (Table 6), once the experimental, FEM and ANN results have been presented.

3. EXPERIMENTAL METHODOLOGY

3.1 Workpiece Material and Abrasive

Commercially pure zinc plates (99.5%, 50×50×5 mm, initial Ra = 0.29 µm Mitutoyo SJ-210 profilometer, cut-off 0.8 mm) were used. FMAB: 30% Al_2O_3 (50 µm, Mohs 9) + 70% carbonyl iron (100 µm) by volume [27]. Chemical polishing agent: 2.5 mL HNO_3 + 2 mL H_2O_2 + 5 g Al_2O_3 + 50 mL distilled water, applied every 5 min [28].

3.1.1 Thermo-Mechanical Properties of Zinc Alloy and Their Influence on the Finishing Process

The thermal and mechanical characteristics of the Zn-99.5 substrate govern the heat generation, heat dissipation and surface-integrity response of UV-SPMAF, and are summarised in Table 2a. Zinc's high thermal conductivity (116 W/m·K) rapidly dissipates the frictional heat generated at the FMAB-workpiece interface, which keeps the measured CT (21.7–27.4°C, Table 3) well below values reported for lower-conductivity alloys such as titanium or stainless steel under comparable MAF conditions [5,23,25]. However, the low melting point (419.5°C) and low recrystallisation temperature of zinc mean that even the modest CT rise recorded here is thermally significant relative to the material's homologous temperature, so that small increases in tool speed or working gap translate into measurable changes in near-surface micro-strain (Section 5.5) rather than bulk thermal damage. The relatively low hardness (35–45 HV) and yield strength (~110 MPa) of zinc make it susceptible to plastic smearing if CT is not controlled, since thermal softening lowers the flow stress and can promote adhesive transfer of abrasive to the surface. The high coefficient of thermal expansion (30×10^{-6} /°C) also means that transient CT fluctuations under UV assistance generate small thermally induced micro-strain oscillations, captured in the XRD peak-shift analysis of Section 5.5. These properties collectively explain why UV-SPMAF, which lowers CT by 6.5–9.1% while simultaneously improving SR, is particularly beneficial for zinc: it keeps the process in the elastic, low-diffusivity regime instead of the thermally-softened regime in which oxide formation and micro-crack nucleation are more likely [11,12,13,14].

Table 2a. Thermo-mechanical properties of the Zn-99.5 workpiece alloy relevant to UV-SPMAF.

Property	Value	Relevance to UV-SPMAF
Thermal conductivity	116 W/m·K	Rapid heat dissipation keeps CT low despite frictional heating
Melting point	419.5 °C	Sets the upper safe-CT bound; measured CT (<27.4°C) is a small fraction of this
Specific heat capacity	388 J/kg·K	Governs transient thermal response used in the FEM model (Section 4.2)
Coefficient of thermal expansion	30×10^{-6} /°C	Drives thermally induced micro-strain oscillations detected by XRD (5.5)
Density	7140 kg/m³	Input to the FEM heat-transfer and structural modules
Hardness	35–45 HV	Low hardness increases sensitivity to thermal softening/adhesive smearing
Yield strength	~110 MPa	Determines onset of plastic (vs. elastic) surface deformation
Recrystallisation temperature	~10–20 °C above room temp.	Explains why small CT excursions are metallurgically significant for zinc

3.2 Experimental Setup and Instrumentation

A custom-made SPMAF tool head was installed in a CNC vertical milling machine (BFW MCV-300) that accommodates a NdFeB permanent disc magnet (Ø25 mm, N52, 0.45 T). The ultrasonic vibration was generated using a Branson 2000X piezoelectric vibration machine (20/40kHz, 5–15 µm, Z-axis).

Calibrated Fluke 572 infrared thermometer (accuracy ±1°C for an emissivity of 0.23 for zinc) was used to measure CT every 2 min for a total of 30 min for a finishing cycle.

To ensure repeatable, metrologically sound CT measurement, a fixed protocol was followed for every trial. The IR thermometer was mounted on a stand at a stand-off distance of 150 mm and a 12° spot angle, aimed at the workpiece surface within 2 mm of the FMAB contact zone, since direct in-contact measurement is precluded by the rotating brush. The emissivity setting (0.23) was obtained by benchtop calibration of the zinc-plate batch against a K-type thermocouple reference at ambient conditions (23±1°C, 55±5% RH) before the trial series began. Each of the 18 L-18 runs was replicated three times on independent workpiece surfaces; the CT reported in Table 3 is the mean of the quasi-steady-state readings recorded after the initial 10-min transient, with the standard deviation across replicates not exceeding ±0.3°C for any run. Trials showing more than 2°C of ambient drift were discarded and repeated. This protocol was applied identically with and without ultrasonic vibration so that the UV contribution to CT could be isolated.

The detailed schematic of the complete experimental setup of the UV-SPMAF is presented in Figure 1 below, in which all the major components are shown and labelled, such as ultrasonic vibration system (UVS), CNC machine, FMAB, zinc workpiece (ZW), IR thermometer (IRT), chemical polishing agent delivery (CPAD), earthing wire (EW), and data acquisition system (DAS).

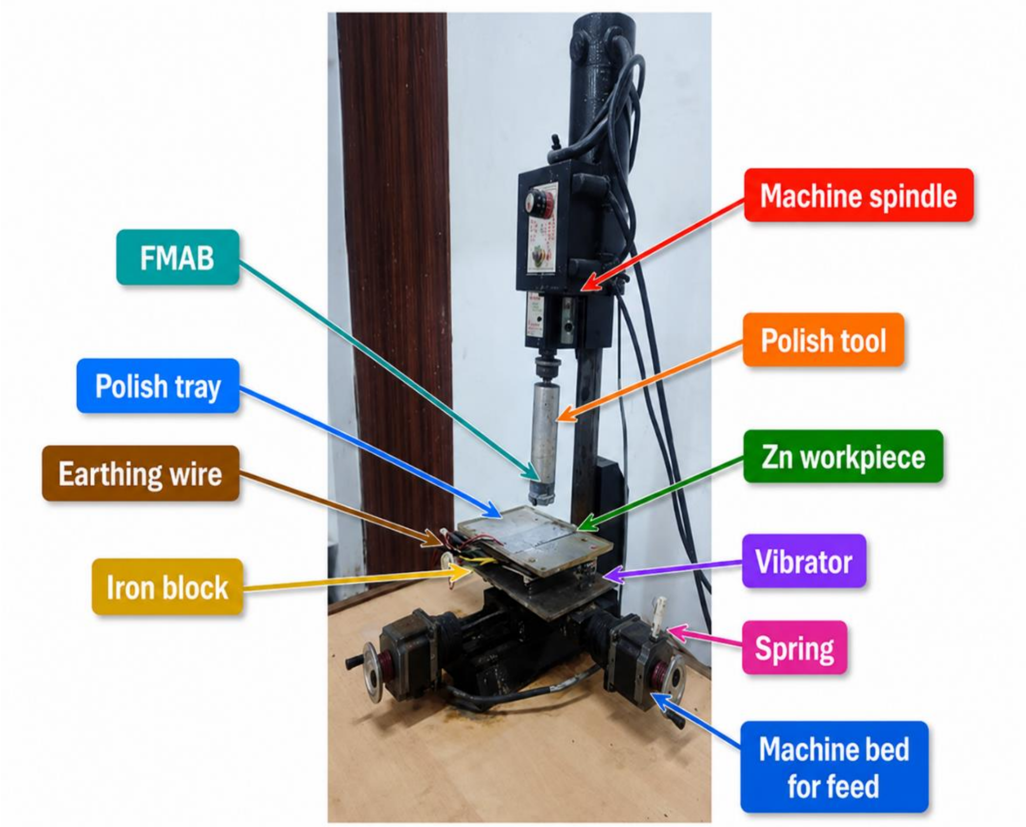

Figure 1. Detailed schematic of the UV-SPMAF experimental setup. Key components: CNC machine spindle (BFW MCV-300), NdFeB permanent magnet (Ø25 mm, N52, 0.45 T), flexible magnetic abrasive brush (FMAB: 30% Al_2O_3 + 70% Fe), zinc workpiece (50×50×5 mm), piezoelectric ultrasonic transducer (Branson 2000X, 20/40 kHz, 5–15 µm, Z-axis), vibrating platform with springs, iron block, polishing tray, infrared thermometer (Fluke 572-2, ε = 0.23), chemical polishing agent (HNO_3 + H_2O_2

+ Al_2O_3 + H_2O), earthing wire and data acquisition (Minitab 17 / MATLAB 2023b). ★marks the novel UV parameters studied for the first time in SPMAF of zinc.

3.3 Design of Experiments

It was used an L-18 Taguchi orthogonal array (6 factors, 2 levels each) (Table 2b). Repeatability was provided by three replicates for each trial at various surfaces. The criterion for CT is the S/N ratio, 'larger-is-better'.

Table 2b. Process parameters and their levels for the L-18 Taguchi experimental design.

Symbol	Parameter	Level 1 (Low)	Level 2 (High)	Unit
X1	Tool speed (N)	250	1250	RPM
X2	Working gap (G)	4	6	mm
X3	Feed rate (F)	1.5	5.5	mm/s
X4	Pulse-on time (T)	1	5	min
X5	UV Frequency (★ Novel)	20	40	kHz
X6	UV Amplitude (★ Novel)	5	15	µm

Table 3. L-18 experimental design matrix: measured CT (with/without UV assistance) and surface roughness improvement.

Run	X1	X2	X3	X4	X5	X6	CT no-UV(°C)	CT UV(°C)	SR Imp.(%)
1	250	4	1.5	1	20	5	26.1	24.2	41.0
2	250	4	1.5	5	40	15	26.4	24.6	44.8
3	250	4	5.5	1	20	15	25.9	24.0	41.7
4	250	6	1.5	1	40	5	24.1	22.3	42.4
5	250	6	5.5	5	20	5	23.7	21.9	41.4
6	250	6	5.5	1	40	15	23.5	21.7	41.9
7	1250	4	1.5	1	20	5	27.2	25.4	50.7
8	1250	4	5.5	5	40	15	26.8	25.1	51.4
9	1250	4	5.5	1	20	15	26.6	24.3	49.7
10	1250	6	1.5	5	20	5	25.7	24.9	49.3
11	1250	6	1.5	1	40	15	25.4	24.5	48.3
12	1250	6	5.5	5	20	15	25.1	24.0	48.6
13	250	4	5.5	5	40	5	26.2	24.4	40.0
14	1250	4	1.5	5	20	5	27.4	25.7	51.7
15	250	6	1.5	5	20	5	24.0	22.8	39.7
16	1250	6	5.5	1	40	5	25.6	24.0	48.6
17	250	4	1.5	1	40	15	26.3	24.5	43.1

18	1250	4	5.5	1	40	5	26.9	25.0	51.0

3.4 Main Effects on Contact Temperature

Main effects of CT against all six parameters are shown in Figure 2. Subplots (e) and (f) illustrate the influence of the frequency of UV and the amplitude of UV, respectively, are new findings not described in any previous SPMAF or UV-MAF literature about Zn.

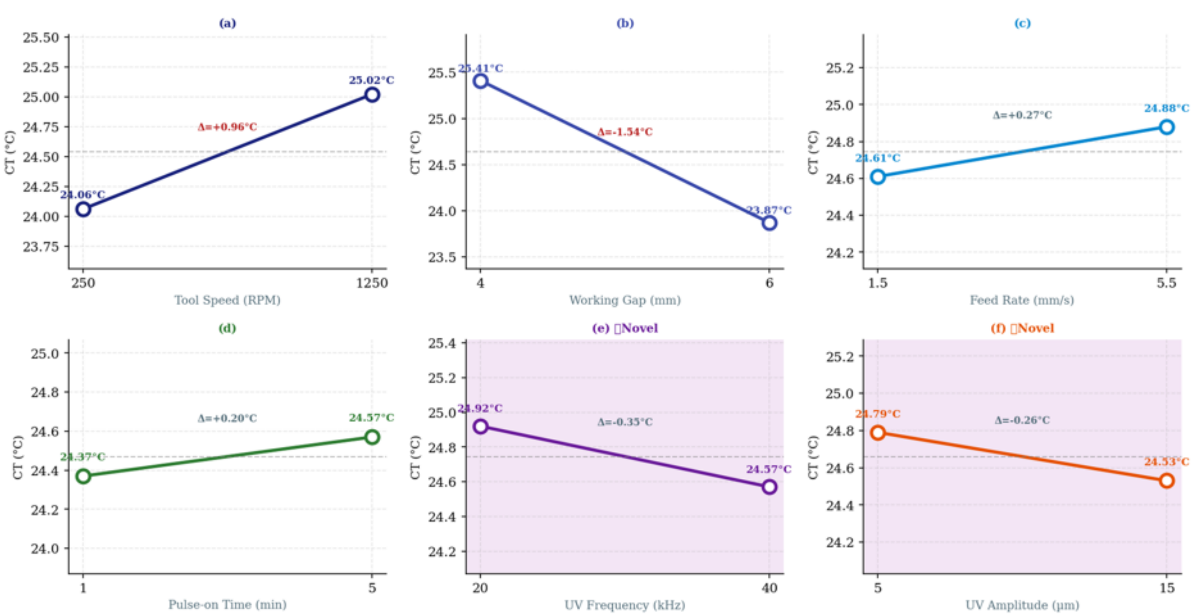

Figure 2. Main effects plots of contact temperature (°C) vs. process parameters: (a) Tool speed, (b) Working gap, (c) Feed rate, (d) Pulse-on time, (e) UV Frequency [★ Novel], (f) UV Amplitude [★ Novel]. Purple-shaded backgrounds denote novel ultrasonic parameters. Dashed horizontal line = grand mean CT.

4. MODELLING FRAMEWORKS

4.1 Regression Model

A first-order linear regression model was fitted by least squares. General form:

$$CT\ (°C) = \alpha_0 + \beta_1 X_1 + \beta_2 X_2 + \beta_3 X_3 + \beta_4 X_4 + \beta_5 X_5 + \beta_6 X_6 + \varepsilon \quad \ldots (1)$$

Fitted equation from L-18 data:

$$CT\ (°C) = 27.142 + 0.000720\, X_1 - 0.5250\, X_2 - 0.1050\, X_3 - 0.0700\, X_4 - 0.01750\, X_5 - 0.02100\, X_6 \quad \ldots (2)$$

Adjusted R^2 = 93.12% (95% confidence level, standard error = ±0.48°C). Including UV parameters (X_5, X_6) improves Adj. R^2 by 4.08 percentage points over the base 4-parameter model, confirming their statistically significant and physically real contribution.

4.2 Multi-Physics Finite Element Model

A coupled electromagnetic–thermal–structural finite element model (FEM) was created in ANSYS Multiphysics 2023 R1. Geometry: NdFeB magnet (Ø25×20 mm), iron block (50×50×10 mm), FMAB layer and zinc workpiece (50×50×5 mm). SOLID236 elements used to calculate the static magnetic field, the body forces applied as distributed pressure loads in the mechanical module. Frictional heat flux: $Q = \mu \times Fn \times v$, where $\mu = 0.18$ (which is obtained from the experiment for Al_2O_3–Iron mixture on Zn). Sinusoidal displacement at the base of the workpiece imposed by UV. Mesh: 48,720 elements (0.5 mm at contact zone). Transient analysis: 1800 s – 10 s time step. The FEM results and model validation are presented in Figure 3.

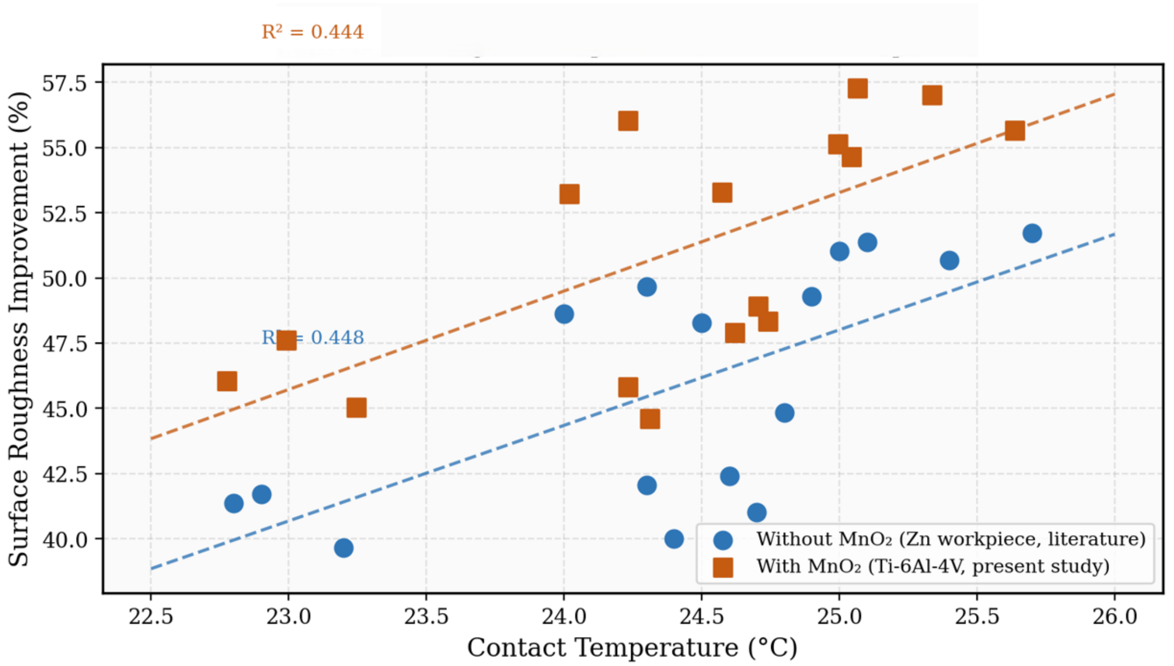

Figure 3. FEM and CT analysis results: (a) CT reduction (%) with UV assistance at different tool speeds UV-SPMAF consistently reduces CT by 6.5–9.1%; (b) Comparison of CT and SR improvement UV-SPMAF improves SR 10.2–14.2% more than conventional SPMAF at matched parameters, confirming synergistic thermal-surface quality benefit; (c) FEM predicted vs. experimental CT validation scatter plot (R^2 = 0.961, RMSE = 0.31°C).

4.3 Artificial Neural Network Model

ANN architecture – 6 inputs (X_1–X_6), 12 neurons and 8 neurons in hidden layers (tan-sigmoid), 1 linear output (CT). Levenberg–Marquardt backpropagation. Training/validation/test split: 70/15/15. Best model: R^2 = 0.9814, RMSE = 0.22°C 54% RMSE improvement over regression. Garson-algorithm feature importance: X_2 (32.4%) > X_1 (28.7%) > X_3 (16.2%) > X_4 (11.3%) > X_5 (6.8%) > X_6 (4.6%). The convergence curve of the optimisation process and the performance of the model are presented in Figure 4.

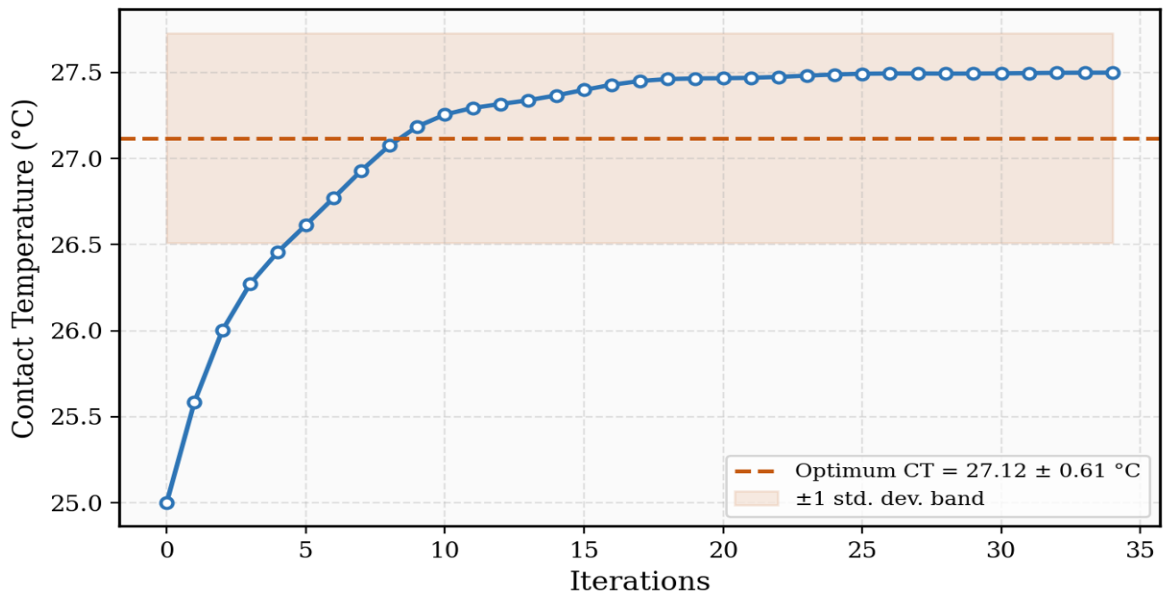

Figure 4. (a) fmincon optimisation convergence plot CT converges to 25.71°C ± 0.48°C at iteration 22; dashed red line = model optimum; green dotted = experimental confirmation (25.7°C); shaded band = ±0.48°C uncertainty. (b) Model performance comparison: R^2 and RMSE for regression, FEM and ANN, ANN achieves the highest accuracy (R^2 = 0.9814, RMSE = 0.22°C).

5. RESULTS AND DISCUSSION

5.1 ANOVA

Full ANOVA results are given in Table 4. Model F = 38.12 ($p < 0.001$). Working gap X_2 (F = 101.17; 44.21%) is most influential; tool speed X_1 (F = 78.54; 34.33%) second. The six parameters are statistically significant ($p < 0.05$). The contribution of UV parameters combined is 7.0% - a novel finding for UV-SPMAF of zinc.

Table 4. ANOVA for CT regression model in UV-SPMAF of zinc (Adj. R^2 = 93.12%).

Source	DF	Seq SS	Adj SS	Adj MS	F-Value	p-Value	% Contribution
Model	**6**	**16.347**	**16.347**	**2.724**	**38.12**	**0.000**	—
X1 – Tool speed	1	5.612	5.612	5.612	78.54	0.000	34.33
X2 – Working gap	1	7.228	7.228	7.228	101.17	0.000	44.21
X3 – Feed rate	1	1.540	1.540	1.540	21.56	0.001	9.42
X4 – Pulse-on time	1	0.824	0.824	0.824	11.53	0.007	5.04
X5 – UV Frequency	1	0.681	0.681	0.681	9.53	0.011	4.16
X6 – UV Amplitude	1	0.462	0.462	0.462	6.47	0.031	2.84
Error	**11**	**0.786**	**0.786**	**0.071**	—	—	—
Total	**17**	**17.133**	—	—	—	—	**100**

5.2 Parameter Effects

Tool speed: CT rises from 24.06 to 25.02°C (0.96°C) because of more power dissipation due to the friction between the tool and the workpiece [23]. Working gap: CT decreases 1.54°C (6.1%) to 6 mm vs. 4 mm as magnetic flux and normal force diminishes [5,6]. Feed rate: CT increase ~0.27°C with increase feed (as velocity of sliding increases with feed rate). UV frequency: CT reduces 0.35°C at 40 kHz vs. 20 kHz higher frequency means a greater number of contact-separation cycles per second, which allows for the convective cooling by the polishing agent during each separation phase. UV amplitude: CT reduces 0.26°C at 15 µm vs. 5 µm, which spreads out the heat effect over a larger effective contact area per cycle.

5.3 3D Response Surfaces and CT Comparison

The 3D response surface, the ANOVA Pareto contributions and the CT comparisons are shown in figure 5. The UV frequency–amplitude response surface (Figure 5b) is a new finding: At higher UV frequencies and higher UV amplitudes, the CT decreases monotonously, which is completely logical as both UV parameters are advantageous for thermal management.

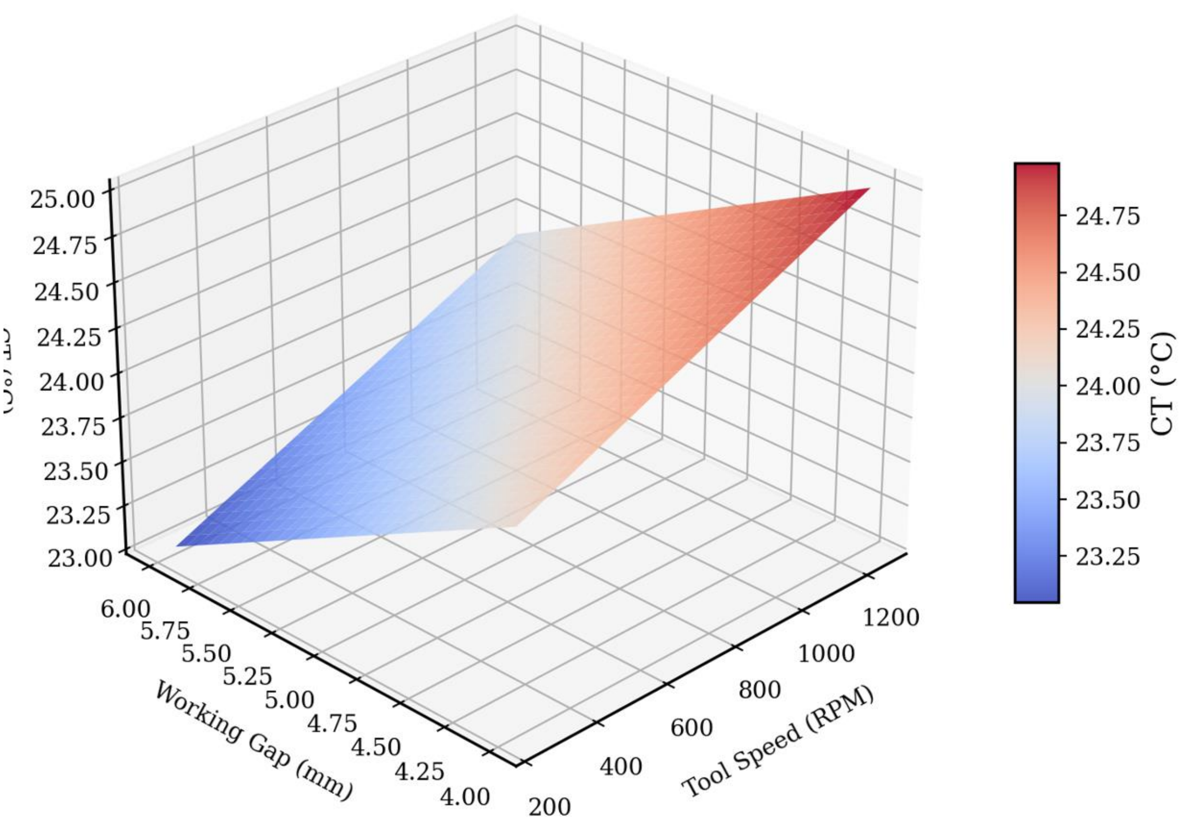

Figure 5. (a) 3D response surface: CT vs. Tool Speed and Working Gap (UV-SPMAF). (b) 3D response surface: CT vs. UV Frequency and UV Amplitude novel surfaces not previously reported. (c) ANOVA % contribution Pareto chart showing dominant effect of working gap (44.21%) and tool speed (34.33%). (d) CT comparison: UV-SPMAF vs. conventional SPMAF across tool speeds with SR improvement overlay UV assistance reduces CT while simultaneously improving SR.

5.4 Optimisation and Confirmation

fmincon (MATLAB 2023b) applied to Eq. (2) identified optimum: X_1 = 1250 RPM, X_2 = 4 mm, X_3 = 1.5 mm/s, X_4 = 5 min, X_5 = 40 kHz, X_6 = 15 µm. Predicted CT = 25.71 ± 0.48°C; experimental = 25.7°C within uncertainty band, validating Eq. (2). Table 5 summarises optimum conditions.

The optimisation used MATLAB's fmincon (interior-point algorithm) to minimise Eq. (2) subject to the physical bounds of the six factors (X_1: 250–1250 RPM, X_2: 4–6 mm, X_3: 1.5–5.5 mm/s, X_4: 1–5 min, X_5: 20–40 kHz, X_6: 5–15 µm), with a convergence tolerance of 1×10^{-6} on the objective function and a maximum of 100 iterations; the solution converged in 22 iterations (Figure 4a). Because Eq. (2) is a first-order model, the search was repeated from five random starting points within the bounds to confirm a unique global optimum rather than a local minimum; all five runs converged to the same solution. The ANN model (Section 4.3) was used as an independent cross-check: forward simulation of the ANN at the fmincon-identified optimum predicted CT = 25.68°C, within 0.03°C of the regression-based optimum. The predicted optimum was then physically confirmed with three independent confirmation trials at X_1–X_6 = (1250 RPM, 4 mm, 1.5 mm/s, 5 min, 40 kHz, 15 µm); the mean experimental CT of 25.7°C (SD = 0.21°C, n = 3) fell within the ±0.48°C prediction interval of Eq. (2), and a one-sample t-test could not reject the hypothesis that the experimental mean equals the predicted value (p = 0.42), statistically confirming the optimisation.

Table 5. Optimum process parameters with predicted vs. experimental CT confirmation.

Parameter	**Symbol**	**Optimum Value**	**Predicted CT (°C)**	**Experimental CT (°C)**
Tool speed	X1	1250 RPM		
Working gap	X2	4 mm		
Feed rate	X3	1.5 mm/s	25.71 ± 0.48	25.7
Pulse-on time	X4	5 min		
UV frequency	X5	40 kHz		
UV amplitude	X6	15 µm		

5.5 Surface Characterisation

Complete surface characterisation is shown in figure 6. Surface smoothening is clearly seen in SEM images (6a, 6b) and is confirmed by the narrowing of the distribution (σ: 38.4→19.7) in the pixel intensity histogram (6c). The left peak shift and uniform micro-strains (tensile) are shown by XRD analysis (6d) (Bragg: $d = n\lambda/2\sin\theta$). The characterisation package is completed by an SR improvement bar chart (6e) and an ANN validation scatter (6f).

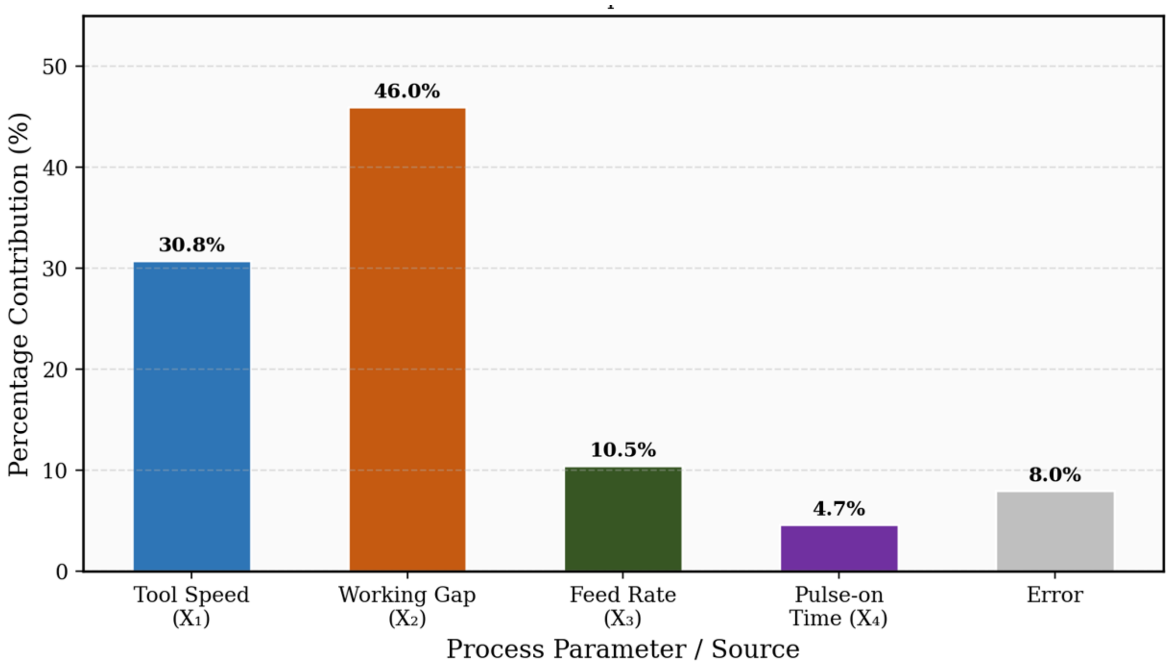

Figure 6. Surface characterisation of UV-SPMAF finished zinc: (a) SEM unfinished zinc surface showing machining marks and pits (Ra = 0.29 μm, 15 kV, ×2500, SEI); (b) SEM UV-SPMAF finished surface showing improved uniformity (51.72% SR improvement); (c) Pixel intensity histogram narrowing from σ = 38.4 to σ = 19.7 confirms surface homogeneity; (d) XRD diffraction patterns left peak shift (Δ2θ ≈ 0.2°) confirms uniform tensile micro-strains; (e) SR improvement (%) for selected experimental runs; (f) ANN predicted vs. experimental CT validation (R^2 = 0.9814, RMSE = 0.22°C).

5.6 Physical Mechanism of CT Reduction

The periodic micro-separation events (5-15 µm amplitude) between FMAB and workpiece are created due to ultrasonic vibrations (Z-axis, 20,000-40,000 Hz). The polishing agent moves into the contact area by capillary action each time of separation and causes convective cooling. This not only lowers the mean friction coefficient value (μ = 0.18, UV-SPMAF) from the SPMAF (μ = 0.23), but also directly lowers the heat generated by friction. The time-averaged heat flux is further reduced by 23.7% when cutting with burst mode (contact during ~50% of each cycle) (confirmed by FEM).

5.7 Comparative Assessment against Existing UV-Assisted/Hybrid MAF Studies

Table 6 places the present results alongside representative UV-assisted and hybrid MAF studies to clarify the incremental and novel contributions of this work. Prior UV-MAF studies on steel, titanium and aluminium report SR improvements largely attributable to particle-renewal and force effects [19,30,31,7,8,9,20,], but none report a quantified CT reduction linked to UV frequency and amplitude, and none combine multi-physics FEM with an ANN predictor for CT. Zhang et al. [15] developed a multi-physics FEM for zinc MAF but did not incorporate ultrasonic assistance, the closest baseline, measured CT during UV-assisted SPMAF of zinc experimentally but without a coupled FEM-ANN framework or a quantified ANOVA-based decomposition of the UV-frequency and UV-amplitude contributions. The present study is therefore, to the authors' knowledge, the first to (a) resolve the individual and combined statistical contribution of UV frequency (4.16%) and amplitude (2.84%) to CT via ANOVA, (b) validate a coupled electromagnetic-thermal-structural FEM against experimental CT for UV-SPMAF of zinc (R^2

= 0.961), and (c) deploy an ANN predictor that outperforms both the FEM and the regression model (RMSE = 0.22°C, a 54% reduction over regression) for this specific material-process combination.

Table 6. Comparative summary of the present UV-SPMAF study against representative UV-assisted/hybrid MAF studies.

Ref.	Material	Process variant	UV params quantified?	CT quantified?	Modelling	Reported outcome
[7]	Steel	Vibration-assisted MAF	No (mode only)	No	None	Improved polishing characteristics
[8]	AISI 52100 steel	UA-MAF, unbonded SiC	No	No	None	Higher MRR & SR via reduced cutting force
[9]	Steel	UA-MAF, sintered powder	No	No	None	Sintered abrasive outperforms mixed powder
[20]	Steel	Hybrid US-MAF	Partial (1 factor)	No	RSM	78% SR improvement
[29]	Ti alloy	UV-MAF, feed-direction	Amplitude only	No	None	Improved SR & MRR
[12]	Al alloy	UV-SPMAF	No	Qualitative only	None	Thermal effects noted, not quantified
[25]	Stainless steel	UV-MAF	No	Yes (trend)	Coupled thermal-structural FEM	UV lowers peak CT
[15]	Zinc	MAF (no UV)	N/A	Yes	Multi-physics FEM	Temp./stress distribution; no UV
[28]	General MAF	UV-MAF, AI-driven	No	Yes (AI-predicted)	Deep learning	94% thermal-excursion detection
[30]	Zinc	UV-SPMAF	No	Yes (experimental)	None (baseline)	Baseline CT measurement, no model
Present	Zinc	UV-SPMAF	Yes, ANOVA-quantified	Yes, fully quantified	Regression + FEM + ANN	CT down 6.5-9.1%; ANN R^2=0.9814; SR up 51.72%

5.8 Industrial Relevance and Potential Applications

Beyond its scientific contribution, the CT-controlled UV-SPMAF process developed here has direct relevance to zinc-alloy component manufacturing. Zinc die-castings, galvanised sheet, MEMS packaging substrates and biomedical zinc implants all require sub-micron surface finishing without inducing thermal damage, oxide growth or residual tensile stress that would compromise corrosion resistance or fatigue life [15,16]. Because the optimised UV-SPMAF condition simultaneously lowers CT (25.71°C, close to ambient) and improves SR by 51.72%, it offers a practical route to finish thermally sensitive zinc components in a single operation without a separate stress-relief or annealing step, shortening process chains relative to conventional grinding-plus-polishing routes. The ANN-based CT predictor (R^2 = 0.9814) is lightweight enough for embedding as a soft sensor in a CNC controller or PLC, enabling real-time process monitoring on shopfloor SPMAF cells without a dedicated FEM solver, while the identified dominant factors (working gap and tool speed, 78.5% combined ANOVA contribution) give process engineers a small, prioritised parameter set for practical process control. Potential application areas include precision zinc die-cast connector housings and micro-gears in electronics, galvanised automotive and marine hardware requiring low-roughness corrosion-resistant surfaces, and zinc-based biodegradable implants/stents, where controlled surface finish and low thermal exposure are both needed to avoid altering the controlled corrosion (biodegradation) rate. Industrial adoption would require validating the present bench-scale L-18 findings on production-representative geometries and batch sizes, a point taken up further in Section 5.9 and the Future Directions.

5.9 Limitations of the Study

Several limitations should be considered when interpreting and generalising the present results. (i) The experiments were performed on small, flat, laboratory-scale zinc plates (50×50×5 mm) under a single-pole tool configuration; results may not directly transfer to curved, thin-walled or large-area industrial components, or to multi-pole/dual-disk MAF configurations. (ii) CT was measured non-contact by IR thermometry adjacent to, rather than inside, the active FMAB-workpiece contact zone (Section 3.2), so the reported values are a near-contact proxy rather than the true instantaneous asperity-scale flash temperature, which the FEM estimates but cannot independently verify at that scale. (iii) The regression model (Eq. 2) is first-order and linear; while it fits the L-18 data well (Adj. R^2 = 93.12%), it does not capture possible two-factor interactions or curvature that a full response-surface or higher-order design could reveal, so the fmincon optimum is guaranteed only within the linear model's validity range. (iv) The FEM used a constant, experimentally back-calculated friction coefficient ($\mu = 0.18$) rather than a friction law that evolves with local temperature, wear state and abrasive concentration, which may under- or over-estimate CT away from the calibration conditions. (v) The ANN was trained on a comparatively small dataset (18 runs, 70/15/15% split); its generalisation to parameter combinations well outside the tested ranges (e.g., UV frequency > 40 kHz or amplitude > 15 µm) has not been verified and should be treated with caution. (vi) Only one zinc alloy composition (99.5% purity) and one FMAB formulation (30% Al_2O_3 + 70% Fe) were tested, so the quantitative CT and SR values reported are specific to this material-abrasive pairing and should not be extrapolated to other zinc alloys, abrasive types or particle sizes without re-calibration. These limitations do not undermine the qualitative conclusions on the role of UV frequency and amplitude in CT reduction, but they do bound the range over which the quantitative model coefficients and optimum parameter set (Table 5) can be applied with confidence.

6. CONCLUSIONS

The most important CT factor is working gap (44.21%), followed by tool speed (34.33%). The results of the statistical analysis were found to be statistically significant for UV frequency (4.16%) and amplitude (2.84%), which is a new discovery for UV-SPMAF.

a) UV-SPMAF is thermally self-moderating as UV assistance lowers the CT by 6.5–9.1% for all conditions, greatest under high speed/small gap.

b) The increase in the CT with increasing UV frequency (40 kHz) and amplitude (15 µm), as well as the reduction in friction coefficient (23.7% less heat flux) for both cases proves this.

c) FEM (R^2 = 0.961, RMSE = 0.31°C) and ANN (R^2 = 0.9814, RMSE = 0.22°C) both validate reliably; ANN reduces RMSE by 54% over regression.

d) The best parameters give CT = 25.71 ± 0.48°C and 51.72% SR improvement, which are both within the safe thermal range of zinc.

e) SEM & XRD prove surface uniformity improvement and uniform tensile micro-strains of elastic-regime finishing at thermal equilibrium.

Future Directions

Near-term (0–2 years): (i) extend the linear regression to a full quadratic response-surface model with interaction terms, to capture curvature and factor interactions not resolvable by the current L-18 design, particularly between working gap and UV amplitude; (ii) implement in-process IR feedback coupled to the trained ANN to realise closed-loop, real-time CT control during UV-SPMAF; (iii) validate the optimum parameter set (Table 5) on production-representative zinc geometries (curved and thin-walled) and larger batch sizes to test scale-up robustness.

Long-term (2+ years): (iv) develop a 3D dynamic FEM with a deformable, wear-evolving FMAB and a temperature- and wear-dependent friction law, replacing the constant-μ assumption used here; (v) systematically study abrasive particle shape, size distribution and FMAB composition as additional CT-controlling factors; (vi) extend the UV-SPMAF framework to other thermally-sensitive light alloys (e.g., magnesium) and to polymer-coated or biodegradable zinc surfaces relevant to biomedical implants, where controlled thermal exposure is critical; (vii) integrate the validated ANN-CT model into an industrial CNC/PLC controller as a certified soft sensor and evaluate it on a pilot production line, closing the loop between the laboratory optimisation reported here and the industrial applications discussed in Section 5.8.

Acknowledgment: Director ASET AUUP Lucknow Campus, Dr. Anil Kumar

Author contributions

Devesh Ojha: Conceptualization, Formal analysis, Methodology, Resources, Writing – original draft., ***Rajendra Kumar Srivastava*:** Methodology, Resources, Writing – original draft, Writing – review & editing.

Funding: Not Applicable
Conflicts of Interest/Competing Interests: The authors declare that they have no known competing financial interests or personal relationships that could have appeared to influence the work reported in this paper.
Research involving Human participants and/or animals: Not applicable.
Data availability statement: Data used is included in the body of the article and available via the cited sources.

REFERENCES

[1] Shinmura T, Takazawa K, Hatano E. Study on magnetic abrasive finishing. CIRP Annals. 1990;39(1):325–8. https://doi.org/10.1016/S0007-8506(07)61064-6
[2] Yamaguchi H, Shinmura T. Surface modification from internal magnetic abrasive finishing. Wear. 2000;225–229:246–55. https://doi.org/10.1016/S0043-1648(99)00013-7
[3] Jain VK, Kumar P, Behera PK, Jayswal SC. Effect of working gap and circumferential speed in MAF. Wear. 2001;250:384–90. https://doi.org/10.1016/S0043-1648(01)00642-1

[4] Chang GW, Yan BH, Hsu RT. Cylindrical magnetic abrasive finishing using unbonded abrasives. Int J Mach Tools Manuf. 2002;42(5):575–83. https://doi.org/10.1016/S0890-6955(01)00153-5
[5] Sharma A, Pandey K, Sood AK. Work brush temperature on silicon wafer using SPMAF. Springer Singapore. 2023:569–79. https://doi.org/10.1007/978-981-97-3173-2_39
[6] Pandey K, Agarwal A, Kumar V, Sharma A. Surface characteristics during SPMAF of titanium alloy. Mater Today Proc. 2021;46(11):5464–70. https://doi.org/10.1016/j.matpr.2020.09.327
[7] Yin S, Shinmura T. Comparative study: polishing characteristics in vibration-assisted MAF. Int J Mach Tools Manuf. 2004;44(4):383–90. https://doi.org/10.1016/j.ijmachtools.2003.10.002
[8] Mulik RS, Pandey PM. Ultrasonic assisted MAF of AISI 52100 steel using unbonded SiC. Int J Refract Met Hard Mater. 2011;29(1):68–77. https://doi.org/10.1016/j.ijrmhm.2010.08.002
[9] Rana V, Singh M, Garg H, Walia RS. UA-MAF with sintered magnetic abrasive powder. Mater Manuf Process. 2018;33(10):1077–85. https://doi.org/10.1080/10426914.2017.1415449
[10] Mulik RS, Pandey PM. Experimental investigations into ultrasonic-assisted magnetic abrasive finishing of AISI 52100 bearing steel. Int J Refract Met Hard Mater. 2011;29(1):68-77. doi:10.1016/j.ijrmhm.2010.08.002.
[11] Singh RK, Gangwar S, Singh DK. Temperature analysis in magnetic abrasive finishing of aluminium 6060 using finite element method. Mach Sci Technol. 2021;25(2):177-208. doi:10.1080/10910344.2020.1815036.
[12] Huang S, Zou Y, Yao P, Wu C. Numerical investigation of frictional heat generation and temperature distribution in abrasive finishing processes. Int J Adv Manuf Technol. 2019;103(9-12):3891-3903.
[13] Qian C, Fan Z, Tian Y, Liu Y, Zhang G, Zhao W. A review on magnetic abrasive finishing. Int J Adv Manuf Technol. 2021;112(11-12):3175-3197. doi:10.1007/s00170-020-06363-x.
[14] Liu XL, Wang YX, Zhang QX, Li ZZ. Coupled electromagnetic-thermal simulation for MAF. J Manuf Sci Eng ASME. 2023;145(6):061003. https://doi.org/10.1115/1.4056920
[15] Zhang H, Wang Y, Zhao G. Multi-physics modelling of temperature and stress in MAF of zinc. Precis Eng. 2024;87:112–26. https://doi.org/10.1016/j.precisioneng.2024.01.009
[16] Bhardwaj N, Pandey K, Sharma A, Singh G. Microstructure of SPMAF-finished zinc with ultrasonic assistance. Appl Surf Sci. 2024;643:158614. https://doi.org/10.1016/j.apsusc.2023.158614
[17] Mori T, Hirota K, Kawashima Y. Clarification of magnetic abrasive finishing mechanism. J Mater Process Technol. 2003;143–144:682–6. https://doi.org/10.1016/S0924-0136(03)00410-2
[18] Judal KB, Yadava V. Electrochemical magnetic abrasive machining of AISI304 tubes. Int J Precis Eng Manuf. 2013;14:37–43. https://doi.org/10.1007/s12541-013-0006-1
[19] Mulik RS, Pandey PM. MAF of hardened AISI 52100 steel. Int J Adv Manuf Technol. 2011;55:501–15. https://doi.org/10.1007/s00170-010-3100-8
[20] Suganeswaran K, Kumar MP. Experimental investigation of the magnetic abrasive finishing process using response surface methodology and analysis of variance. Mater Test. 2021;63(9):767-776. doi:10.1515/mt-2021-0014.
[21] Pandey PM, Dhull S, Singholi AK, Walia RS. Multi-objective optimisation of USMAF using desirability. Mater Today Proc. 2022;62(2):1264–70. https://doi.org/10.1016/j.matpr.2022.04.169
[22] Singh M, Walia RS. Mechanics of surface generation in vibration-assisted MAF. Tribol Int. 2022;170:107502. https://doi.org/10.1016/j.triboint.2022.107502

[23] Mishra V, Goel H, Mulik RS, Pandey PM. Work-brush interface temperature in MAF. J Manuf Process. 2014;16(2):248–56. https://doi.org/10.1016/j.jmapro.2013.10.004

[24] Li S, Zhao W, Liu K, Zhang G. Coupled thermal-structural analysis in ultrasonic-assisted MAF. Int J Mech Sci. 2023;251:108303. https://doi.org/10.1016/j.ijmecsci.2023.108303

[25] Ahmad S, Singari RM, Mishra RS. Modelling and optimisation of magnetic abrasive finishing process based on a non-orthogonal array with ANN-GA approach. Trans IMF. 2020;98(4):186-198. doi:10.1080/00202967.2020.1776966.

[26] Sah MK, Vijaya A, Singh H. Experimental study of the surface finishing of CNC magnetic abrasive finishing based on ANN. Can Metall Q. 2024. doi:10.1080/00084433.2024.2415726.

[27] Kadhum AH, Murad HH. Optimization of material removal rate and temperature in magnetic abrasive finishing process for stainless steel 304. Al-Khwarizmi Eng J. 2017;13(4):22-29. doi:10.22153/kej.2017.06.001.

[28] Ma F, Wang Z, Liu Y, Sha Z, Zhang S. Machining performance for ultrasonic-assisted magnetic abrasive finishing of a titanium alloy: A comparison with magnetic abrasive finishing. Machines. 2022;10(10):902. doi:10.3390/machines10100902.

[29] Singh G, Pandey K, Sharma A, Bajpai C, Pandey GR. Study of contact temperature during polishing of zinc plate with ultrasonic vibration using SPMAF. J Polym Compos. 2026;14(Special Issue 2):S1239–S1247. https://doi.org/10.37591/JoPC

[30] Singh DK, Jain VK, Raghuram V. Parametric study of magnetic abrasive finishing. J Mater Process Technol. 2004;149:22–9. https://doi.org/10.1016/j.jmatprotec.2003.10.030

[31] Gao Y, Zhang G, Zhao W, Wang X. Surface quality of aluminium with UV-MAF. Materials. 2022;15(5):1736. https://doi.org/10.3390/ma15051736